Volume 1 | Number 1 | Jan 2013 | Pages 1–100

Journal of
Materials Chemistry A

Materials for energy and sustainability
www.rsc.org/materialsA

ROYAL SOCIETY
OF CHEMISTRY

ROYAL SOCIETY
OF CHEMISTRY

www.rsc.org/materialsA

Journal Name

ARTICLE

Synthesis and Characterization of $(Ga_{1-x}Zn_x)(N_{1-x}O_x)$ Nanocrystals with a Wide Range of Compositions †

Kyureon Lee,[a] Ying-Gang Lu,[a] Chi-Hung Chuang,[a] Jim Ciston,[b] Gordana Dukovic[a]*

We describe the synthesis and characterization of wurtzite $(Ga_{1-x}Zn_x)(N_{1-x}O_x)$ nanocrystals with a wide range of compositions and a focus on properties relevant for solar fuel generation. $(Ga_{1-x}Zn_x)(N_{1-x}O_x)$, a solid solution of GaN and ZnO, is an intriguing material because it exhibits composition-dependent visible absorption even though the parent semiconductors absorb in the UV. When functionalized with co-catalysis, $(Ga_{1-x}Zn_x)(N_{1-x}O_x)$ is also capable of water splitting under visible irradiation. Here, we examine the synthesis of $(Ga_{1-x}Zn_x)(N_{1-x}O_x)$ nanocrystals to understand how they form by nitridation of ZnO and $ZnGa_2O_4$ nanocrystalline precursors. We find that the ZnO precursor is critical for the formation of crystalline $(Ga_{1-x}Zn_x)(N_{1-x}O_x)$ at 650 °C, consistent with a mechanism in which wurtzite $(Ga_{1-x}Zn_x)(N_{1-x}O_x)$ nucleates topotactically on wurtzite ZnO at an interface with $ZnGa_2O_4$. Using this information, we expand the range of compositions from previously reported $0.30 \leq x \leq 0.87$ to include the low-x and high-x ends of the range. The resulting compositions, $0.06 \leq x \leq 0.98$, constitute the widest range of $(Ga_{1-x}Zn_x)(N_{1-x}O_x)$ compositions obtained by one synthetic method. We then examine how the band gap depends on sample composition and find a minimum of 2.25 eV at $x=0.87$, corresponding to a maximum possible solar-to-H_2 power conversion efficiency of 12%. Finally, we examine the photoelectrochemical (PEC) oxidation behavior of thick films of $(Ga_{1-x}Zn_x)(N_{1-x}O_x)$ nanocrystals with $x=0.40$, 0.52, and 0.87 under visible illumination. $(Ga_{1-x}Zn_x)(N_{1-x}O_x)$ nanocrystals with $x=0.40$ exhibit solar PEC oxidation activity that, while too low for practical applications, is higher than that of bulk $(Ga_{1-x}Zn_x)(N_{1-x}O_x)$ of the same composition. The highest photocurrents are observed at $x=0.52$, even though $x=0.87$ absorbs more visible light, illustrating that the observed photocurrents are a result of an interplay of multiple parameters which remain to be elucidated. This set of characterizations provides information useful for future studies of composition-dependent PEC properties of nanoscale $(Ga_{1-x}Zn_x)(N_{1-x}O_x)$.

Introduction

The oxynitride $(Ga_{1-x}Zn_x)(N_{1-x}O_x)$, a solid solution of GaN and ZnO, has drawn considerable interest for solar water splitting since its discovery in 2005.[1] This material is intriguing because its band gap can be tuned down to the visible region by varying the composition (fraction of ZnO, x) even though the parent semiconductors have band gaps in the UV region (3.4 eV for GaN and 3.2 eV for ZnO). The origin of the band gap reduction upon mixing of ZnO and GaN is still under debate.[2-12] Moreover, it has been demonstrated that $(Ga_{1-x}Zn_x)(N_{1-x}O_x)$ can act as a stable visible light driven photocatalyst for overall water splitting into H_2 and O_2 when it is modified with proper co-catalysts.[13-23] The first reported synthesis of $(Ga_{1-x}Zn_x)(N_{1-x}O_x)$ involves nitridation of a mixture of bulk Ga_2O_3 and bulk ZnO at temperatures of 850 °C and above.[1, 14] In this reaction, spinel $ZnGa_2O_4$ forms and serves as an intermediate that converts to $(Ga_{1-x}Zn_x)(N_{1-x}O_x)$ under NH_3 flow.[24] The fraction of ZnO (x) that can be achieved in this synthetic route is limited by the spinel intermediate and high volatility of zinc at the high nitridation temperature. To examine the correlation between band gap and composition, other synthetic methods to make bulk $(Ga_{1-x}Zn_x)(N_{1-x}O_x)$ have been explored.[25-27] Because nanoscale particles can have improved crystallinity and shorter diffusion distances for photoexcited carriers transported to the surface,[28, 29] efforts have also been undertaken to synthesize nanoscale $(Ga_{1-x}Zn_x)(N_{1-x}O_x)$. The earliest reported methods included nanowires as well as ~10 nm nanoparticles with a range of x values from 0.08 to 0.48.[30, 31] We subsequently reported a method for synthesizing $(Ga_{1-x}Zn_x)(N_{1-x}O_x)$ nanocrystals with x values ranging from 0.30 to 0.87.[32] Other methods for synthesis of $(Ga_{1-x}Zn_x)(N_{1-x}O_x)$ nanowires, nanotubes, and hollow nanospheres have since been reported.[33-36]

As described in our previous report,[32] single crystalline $(Ga_{1-x}Zn_x)(N_{1-x}O_x)$ nanoparticles with diameters of ~18 nm and x ranging from 0.30 to 0.87 can be obtained by exposure of a

a. Department of Chemistry and Biochemistry, University of Colorado Boulder, Boulder, Colorado 80309, United States
b. National Center for Electron Microscopy, Molecular Foundry, Lawrence Berkeley National Laboratory, Berkeley, California 94720, United States

mixture of ZnO and $ZnGa_2O_4$ nanocrystals to NH_3 at 650 ^{o}C. The *x* value here refers to the overall molar composition of the sample usually measured by elemental analysis of the metal content, i.e., *x*=Zn/(Zn+Ga). The use of nanoscale precursors allowed us to lower the nitridation temperature from that used in the bulk synthesis[1, 14] and thus avoid the loss of Zn. The *x* values in products were tunable simply by changing the ratios of ZnO and $ZnGa_2O_4$ in the starting material mixture. To understand how properties such as band gap and photoelectrochemical (PEC) activity of nanoscale $(Ga_{1-x}Zn_x)(N_{1-x}O_x)$ depend on composition, it is desirable to obtain a broader range of compositions approaching pure GaN (*x*=0) and ZnO (*x*=1). We have shown that, for nanocrystalline $(Ga_{1-x}Zn_x)(N_{1-x}O_x)$, the absorption onset decreases monotonically from *x*=0.30 to *x*=0.87. However, the minimum band gap necessarily exists at a certain value of *x*, and this minimum value and the associated composition have not been determined. The composition that corresponds to the smallest band gap is the most useful from the standpoint of sunlight absorption. To achieve this broader range of compositions, it is necessary to understand the mechanism of formation of $(Ga_{1-x}Zn_x)(N_{1-x}O_x)$ nanocrystals in the synthesis. Specifically, it is not obvious how the two nanocrystalline oxide precursors, wurtzite ZnO and spinel $ZnGa_2O_4$, combine under NH_3 flow to make wurtzite $(Ga_{1-x}Zn_x)(N_{1-x}O_x)$ at this relatively low temperature. Finally, because $(Ga_{1-x}Zn_x)(N_{1-x}O_x)$ materials are of interest for applications in solar water splitting, it is necessary to assess whether the $(Ga_{1-x}Zn_x)(N_{1-x}O_x)$ in a nanocrystalline form is PEC active.

In this manuscript, we describe the broadest range of composition of $(Ga_{1-x}Zn_x)(N_{1-x}O_x)$ obtained with one synthetic method, encompassing *x* values from 0.06 to 0.98. By examining the temperature-dependence of nitridation of $ZnGa_2O_4$ under NH_3, we found that, at the relatively low synthesis temperature of 650 ^{o}C, inclusion of ZnO in the starting material is necessary to obtain wurtzite $(Ga_{1-x}Zn_x)(N_{1-x}O_x)$. Monitoring the conversion of spinel $ZnGa_2O_4$ to the wurtzite final product under NH_3 over time allowed us to propose a mechanism in which $(Ga_{1-x}Zn_x)(N_{1-x}O_x)$ forms at the interface of ZnO and $ZnGa_2O_4$ by nucleating topotactically on ZnO. With the insights from these experiments, we expanded the range of *x* values at each end (*x*=0.06, 0.24, 0.91, and 0.98). We found that the lowest band gap, 2.25 eV, occurs at *x*=0.87. Little compositional mixing is necessary to achieve visible absorption, which is observed at both ends of the composition range, in agreement with previous observations in bulk $(Ga_{1-x}Zn_x)(N_{1-x}O_x)$,[14, 25, 27, 30, 36, 37] although the appearance of the spectra is qualitatively different at the two ends of the range. Finally, we compared PEC oxidation using thick films of nanoscale $(Ga_{1-x}Zn_x)(N_{1-x}O_x)$ under visible irradiation and found that this material is photoactive, exhibiting higher photocurrent density than its bulk counterpart, albeit still too low for practical applications. The dependence of PEC activity on composition does not scale simply with absorption of visible light, which indicates that the measured photocurrents depend on multiple parameters that remain to be determined. The insights into the mechanism of

formation of $(Ga_{1-x}Zn_x)(N_{1-x}O_x)$ nanocrystals, the expanded composition range, and the optical and PEC properties improve our understanding of this unusual material and provide information useful for future studies of composition-dependent PEC properties of nanocrystalline $(Ga_{1-x}Zn_x)(N_{1-x}O_x)$.

Experimental

$(Ga_{1-x}Zn_x)(N_{1-x}O_x)$ nanocrystal synthesis.

All chemicals were purchased commercially and used without further purification. The starting materials ($ZnGa_2O_4$ and ZnO nanocrystals) were prepared and nitridations were carried out as described previously.[32] Briefly, ZnO (d~10 nm) and 3-mercaptopropionic acid capped $ZnGa_2O_4$ nanocrystals (d~5 nm) were mixed and dispersed in a water/ethanol mixture and dropped onto a glass slide to evaporate the solvent over a hot plate. The starting mixture was then scraped out of the glass slide to gather the uniformly mixed starting mixture. Nitridations were carried out in a tube furnace (Across) with flowing NH_3 (~150 ml/min). The furnace was purged with argon for 1 hour and NH_3 gas for 30 min before increasing temperature with a ramp up speed of 20 ^{o}C/min. After nitridation, the furnace was allowed to cool down to room temperature with flowing NH_3 before removal of the nitrided products.

Characterization.

Powder X-ray diffraction (XRD) patterns were collected with Rigaku Ultima IV diffractometer equipped with Cu Kα radiation (λ=0.1540562 nm). Elemental analysis of Zn and Ga was carried out using an ARL 3410+ inductively coupled plasma-optical emission spectrometer (ICP-OES). Oxygen and nitrogen content were measured using a LECO model TC 600 elemental analyzer. Diffuse reflectance spectra were collected on a Shimadzu UV-3600 spectrophotometer equipped with an integrating sphere. Diffuse reflectance was converted to absorbance using the Kubelka-Munk equation ($A=(1-R_\infty)^2/2R_\infty$; $R_\infty=R_{sample}/R_{reference}$). The reflectance of reference ($R_{reference}$) was obtained using $BaSO_4$ as a reference material. Low-magnification transmission electron microscopy (TEM) images were recorded using a Philips CM100 microscope operated at 80 kV. Annular dark-field scanning transmission electron microscopy (ADF-STEM) was performed on an FEI Titan microscope operated at 200kV. X-ray photoelectron spectra (XPS) for selected nanoscale $(Ga_{1-x}Zn_x)(N_{1-x}O_x)$ samples (*x*=0.40, 0.52 0.76, 0.93) were collected at Evans Analytical Group with a PHI 5802 Multitechnique XPS that is equipped with Al Kα (1486.6 eV) or Mg Kα (1253.6 eV) X-ray sources. Al Kα X-ray source was used for the all XPS spectra except N1s. The XPS spectra for N1s were collected using a Mg Kα X-ray source to avoid the peak interference of Ga Auger lines in the N 1s region. Binding energy was calibrated with C1s at 284.8 eV.

Fabrication of $(Ga_{1-x}Zn_x)(N_{1-x}O_x)$/FTO Electrodes.

Bulk $(Ga_{1-x}Zn_x)(N_{1-x}O_x)$ (*x*=0.40) was synthesized using the originally reported synthetic method[14] in order to compare

with nanoscale $(Ga_{1-x}Zn_x)(N_{1-x}O_x)$. Electrodes were prepared by doctor blading for both bulk and nano-$(Ga_{1-x}Zn_x)(N_{1-x}O_x)$ (x=0.40 for bulk; x=0.40, 0.52, and 0.87 for nano). 0.1 g of ethylcellulose and 10 mL of α-terpineol were mixed thoroughly. 10 mg of this mixture was added to 10 mg of $(Ga_{1-x}Zn_x)(N_{1-x}O_x)$ and mixed by grinding to form a paste. The prepared paste was then applied onto the FTO, the edges of which were covered with tape. The paste on the FTO was flattened with a razor blade by scrapping out the excess paste over the tape. The film was dried at 100 ^{o}C for 10 minutes after removing the tape. The resulting films were annealed at 400 ^{o}C for 1 hour under air to burn out the organics.

Measurement of Visible Light Induced PEC Current from $(Ga_{1-x}Zn_x)(N_{1-x}O_x)$/FTO Electrodes.

A three-electrode cell composed of $(Ga_{1-x}Zn_x)(N_{1-x}O_x)$/FTO working electrode, Pt counter electrode, and Ag/AgCl reference electrode was utilized. A 300 Watt Xe-arc lamp (Newport 67005) was used as the light source. To approximate the intensity of 1 sun, the distance between the working electrode and the light source was adjusted using a $GaP_{0.98}N_{0.02}$ detector to determine the electrode location. The lamp-electrode distance was chosen such that the $GaP_{0.98}N_{0.02}$ detector produced the same current as it does under AM1.5G illumination. Then, the light was passed through a 435 nm long pass filter. The photocurrents were collected from oxidation in pH 4.5 of 0.5 M Na_2SO_4 aqueous solution (pH adjusted using H_2SO_4) and sulfite oxidation in pH 7 phosphate buffer solution with 0.5 M Na_2SO_3. Photocurrent was recorded while scanning the voltage from negative to positive with a rate of 10 mV/s. The light was chopped manually. Wavelength-dependent incident photon-to-current efficiency (IPCE) for sulfite oxidation was measured with the identical three-electrode cell setup in pH 7 phosphate buffer solution with 0.5 M Na_2SO_3. Photocurrents were measured with illumination from 300 Watt Xe-arc lamp (Newport) passed through a monochromator at a potential of 0.5 V vs. RHE. A Si photodiode with known quantum efficiency was used to collect a reference spectrum in the same instrument. The IPCE was calculated as: IPCE (%) = photocurrent × (quantum efficiency of Si reference/reference photocurrent) × 100.

Results and Discussion

1. Formation of $(Ga_{1-x}Zn_x)(N_{1-x}O_x)$ nanocrystals

In order to expand the range of compositions of $(Ga_{1-x}Zn_x)(N_{1-x}O_x)$ nanocrystals beyond 0.30≤x≤0.87, we first closely examined how these materials form by nitridation of a mixture of ZnO (d~10 nm) and $ZnGa_2O_4$ (d~5 nm) nanocrystals under NH_3 at 650 ^{o}C. In the original synthesis of bulk $(Ga_{1-x}Zn_x)(N_{1-x}O_x)$, a mixture of Ga_2O_3 and ZnO is heated under NH_3 at 850 ^{o}C.[1, 13, 14] It has been demonstrated that the spinel $ZnGa_2O_4$ forms from the starting material mixture at 850 ^{o}C under NH_3 and serves as an intermediate that directly converts to wurtzite $(Ga_{1-x}Zn_x)(N_{1-x}O_x)$.[24] This mechanism would lead to a maximum x value of ~0.3 without an additional Zn source,

although the values achieved at such a high temperature are lower because of evaporation of Zn.[22, 24, 26] By using nanocrystalline precursors, we were able to lower the reaction temperature by 200 ^{o}C and avoid the loss of Zn.[32] We attributed this lowering of required temperature to the higher surface energy and smaller diffusion distances for the solid state conversion when nanoscale precursors are used. Interestingly, however, nitridation of pure $ZnGa_2O_4$ nanocrystals under these conditions (650 ^{o}C for 10 hrs) does not lead to a crystalline wurtzite product, but rather to a material with one very broad peak in the XRD pattern and a similar value of Zn/(Zn+Ga) as the starting material (Figure 1). This could correspond to an amorphous material or one with very small spinel domains.[38, 39] By increasing the temperature to 750 ^{o}C, we see formation of wurtzite with broad peaks indicating a small crystalline domain size. Because of the increased temperature, we see a significant decrease in Zn/(Zn+Ga) due to loss of Zn. At 850 and 950 ^{o}C, this effect is even stronger, with well-defined wurtzite peaks but very small values of Zn/(Zn+Ga) (<0.03). From the data in Figure 1, we conclude that, under our experimental conditions, crystalline wurtzite $(Ga_{1-x}Zn_x)(N_{1-x}O_x)$ nanocrystals cannot be prepared at 650 ^{o}C from $ZnGa_2O_4$ nanocrystals alone. To prepare crystalline wurtzite nanoscale $(Ga_{1-x}Zn_x)(N_{1-x}O_x)$, addition of ZnO nanocrystals is required. Thus, in addition to serving as a source of Zn in the final product, ZnO plays a critical role in the product crystallinity. It has been shown in bulk $(Ga_{1-x}Zn_x)(N_{1-x}O_x)$, with synthesis temperatures of 850 ^{o}C and above, that the presence of ZnO in the starting material mixture improves the crystallinity of the final $(Ga_{1-x}Zn_x)(N_{1-x}O_x)$ product, as well as increasing the x value of the product.[22, 40]
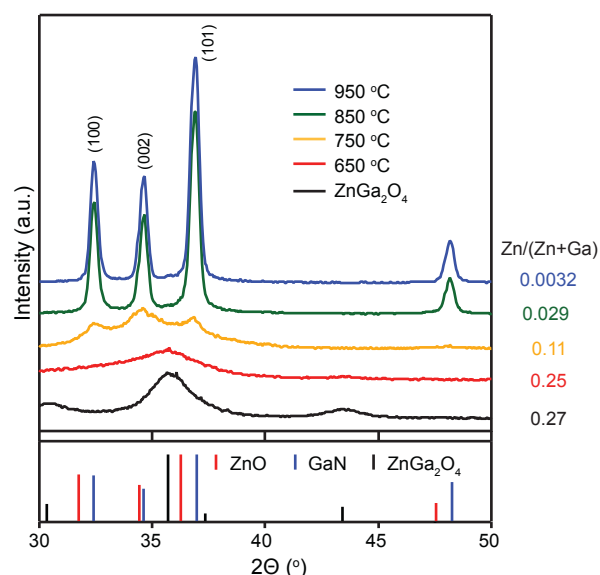

Figure 1. Powder XRD patterns of the products obtained from nitridation of $ZnGa_2O_4$ nanocrystals for 10 hours at varying reaction temperatures. The pattern of the $ZnGa_2O_4$ nanocrystals before nitridation is shown in black. The vertical lines represent the reference diffraction patterns of $ZnGa_2O_4$ (black, JCPDS #38-1240), ZnO (red, JCPDS #05-0664), and GaN (blue, JCPDS # 2-1078).

Figure 2. (a) Powder XRD patterns of the products from nitridation of a starting mixture with Zn/(Zn+Ga)=0.39 for 0–16 hours at 650 °C. The vertical lines represent the reference diffraction patterns of ZnGa$_2$O$_4$ (black, JCPDS #38-1240), ZnO (red, JCPD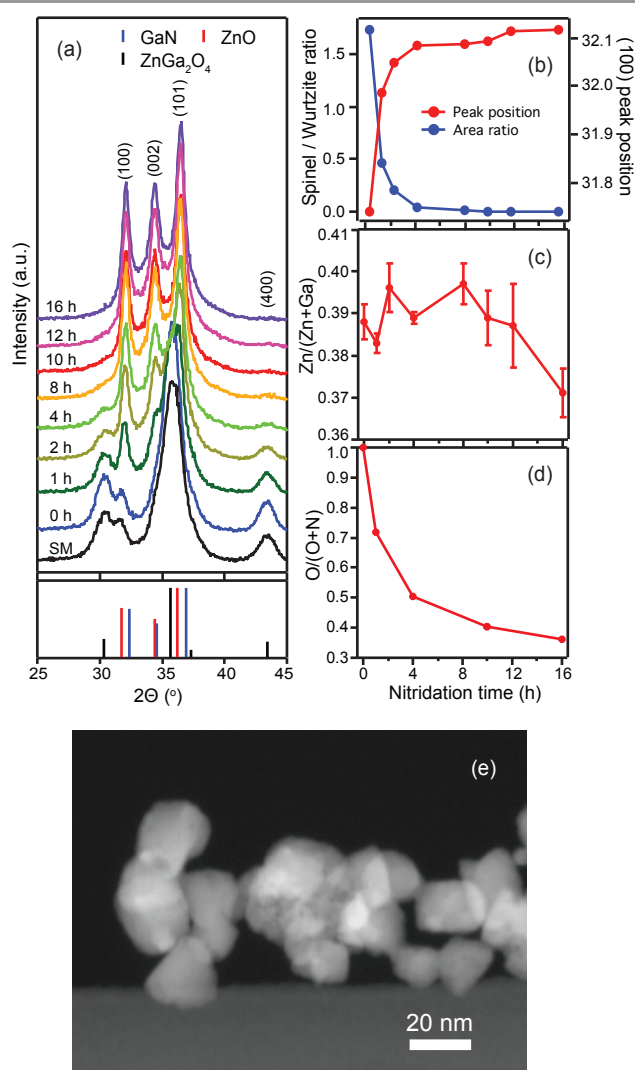S #05-0664), and GaN (blue, JCPDS # 2-1078). (b) Area ratio of (400) spinel peak to (100) wurtzite peak (blue) and position of (100) peak of wurtzite (red). (c) Values of Zn/(Zn+Ga). (d) Values of O/(O+N). (e) ADF-STEM image of the product after 10 hours of nitridation.

Next, we focus on how the spinel ZnGa$_2$O$_4$ in the starting material mixture with ZnO converts to wurtzite at 650 °C. We conducted a set of nitridations with a starting mixture with Zn/(Zn+Ga)=0.39. The starting mixture of ZnO and ZnGa$_2$O$_4$ nanocrystals was nitrided at 650 °C for 0, 1, 2, 4, 8, 10, 12 and 16 hours under flowing NH$_3$. The XRD patterns of the nitrided products are shown in Figure 2a. The starting mixture (SM) displays both wurtzite and spinel peaks attributed to the presence of ZnO and ZnGa$_2$O$_4$, respectively. The changes of ZnGa$_2$O$_4$ during the nitridation were examined via the well-resolved (400) spinel peak appearing at 2Θ=43.4^o since the most intense (311) spinel peak at 2Θ=35.7^o overlaps with the (101) peak of ZnO. The spinel (400) peak quickly decreases in intensity as the nitridation progresses and finally disappears between 8 and 10 hours of nitridation. The XRD patterns of the products from 0–8 hours of nitridation are fit well with a combination of spinel and wurtzite peaks, whereas the 10–16 hours products can be fit with wurtzite reference peaks alone (Figure S1). No intermediate phase was observed. Figure 2b shows the area ratio of the (400) spinel peak to the (100) wurtzite peak as well as the position of the wurtzite (100) peak. As the fraction of the spinel phase decreases, the wurtzite peak shifts from the ZnO value (31.7^o) to the value of the nitrided products (~32.1^o). Figure 2c shows that Zn/(Zn+Ga) does not change appreciably over this time course, indicating that the changes observed in the XRD patterns are not due to loss of Zn. The value of O/(O+N) in the nitrided products is shown in Figure 2d. It decreases from 1 to the O/(O+N) value in the final product as N is incorporated into the product. The product from 10 hours of nitridation had the same values of Zn/(Zn+Ga) and O/(O+N) (0.39 and 0.40, respectively), indicating the (Ga$_{1-x}$Zn$_x$)(N$_{1-x}$O$_x$) synthesis is complete at the time. Figure 2e shows an ADF-STEM image of the product nanocrystals from the sample obtained after 10 hours of nitridation, demonstrating that the synthesis leads to a nanoscale product, as previously reported.[32] The existence of particles with diameters in the 10-20 nm range is in agreement with the crystallite size determined from the XRD pattern in Figure 2a (~17 nm).

The XRD and elemental analysis data in Figure 2 suggest that spinel disappearance, formation of wurtzite (Ga$_{1-x}$Zn$_x$)(N$_{1-x}$O$_x$), and N incorporation occur on a similar timescale with no crystalline intermediates. From Figure 1, we concluded that wurtzite ZnO is necessary for the formation of the wurtzite (Ga$_{1-x}$Zn$_x$)(N$_{1-x}$O$_x$) at 650 °C. From these observations, we propose that at 650 °C wurtzite (Ga$_{1-x}$Zn$_x$)(N$_{1-x}$O$_x$) forms by nucleation at the interface of ZnO and ZnGa$_2$O$_4$, which is facilitated by the similar crystalline lattice of the underlying ZnO. Such topotactic nucleation is well known in solid state reactions.[41] Upon nucleation, the reaction can proceed by diffusion of the atoms of the elements that constitute the product and simultaneous chemical conversion to the oxynitride. Higher temperatures are needed to nucleate (Ga$_{1-x}$Zn$_x$)(N$_{1-x}$O$_x$) from spinel ZnGa$_2$O$_4$ because the starting material is lacking wurtzite structure that aids in product nucleation. The formation of an interface between the ZnGa$_2$O$_4$ (~5nm) and ZnO (~10nm) particles can be seen in the TEM images at various time points in the reaction (Figure S2). The two types of particles exist separately in the starting mixture, appear to fuse together over 0–2 hours of nitridation, and then the fused particles reach their final size from 4 hours of nitridation. This mechanism of the solid state reaction that forms the oxynitride product may result in heterogeneities due to the requirement for an interface between ZnO and ZnGa$_2$O$_4$ to nucleate the product. In the starting material mixture, there may be various interface arrangements. Some of this heterogeneity can be seen as differences in particle size and shape in the TEM images (e.g., Figures 2e and S2). An understanding of such heterogeneities is outside the scope of this manuscript. Thus, we emphasize that in this work, the value of x refers to the value measured by elemental analysis of the overall sample, and may vary from particle to particle.
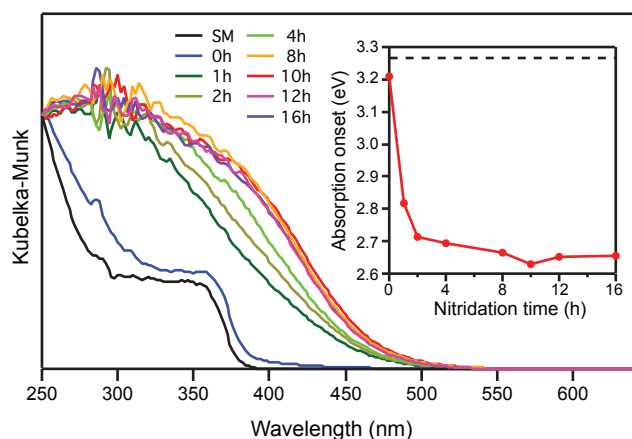
Figure 3. Diffuse reflectance spectra (normalized at 250 nm) of the products of nitridation for 0–16 hours at 650 ^{o}C with Zn/(Zn+Ga)=0.39. Inset shows the absorption onsets of the products as a function of the nitridation time along with that of the starting mixture (SM, dashed line).

Figure 3 shows the diffuse reflectance spectra of the nitrided products from Figure 2 along with that of the starting mixture, demonstrates how the visible absorption develops as the reaction progresses. In the absorption spectrum of the starting mixture, two absorption edges with onsets at 295 nm (4.2 eV) and at 390 nm (3.2 eV) are observed, which correspond to the band gap absorption of $ZnGa_2O_4$[42] and ZnO,[43] respectively. These characteristic features disappear within the first hour of nitridation, and the absorption onsets of the nitrided products significantly shift to lower energy. This occurs at the same time as the changes observed in the XRD patterns and O/(O+N) analysis (Figure 2). After the most significant changes within the first hour of nitridation, the spectra continue to red shift with reaction time up to 10 hours with formation of $(Ga_{1-x}Zn_x)(N_{1-x}O_x)$. The absorption spectra provide an indication for determining an optimized nitridation time for the reaction. The absorption onsets decrease until 10 hours of nitridation, and increase after then due to a small loss of Zn, consistent with the elemental analysis in Figure 2c. This suggests that 10 hours of nitridation is optimal. At that time, the values of Zn/(Zn+Ga) and O/(O+N) are equal (Figure 2c,d).

We conducted a similar set of nitridation-time dependent experiments for a ZnO-rich $(Ga_{1-x}Zn_x)(N_{1-x}O_x)$ synthesis (x=0.78) (Figure S3). We observed similar behavior, with a faster disappearance of $ZnGa_2O_4$ and a smaller shift in the position of the (100) wurtzite peak during the reaction, as the final product is ZnO-rich. This similarity in behavior suggests that the reaction mechanism studied with the low-ZnO samples (x=0.39) is valid for the ZnO-rich samples as well.
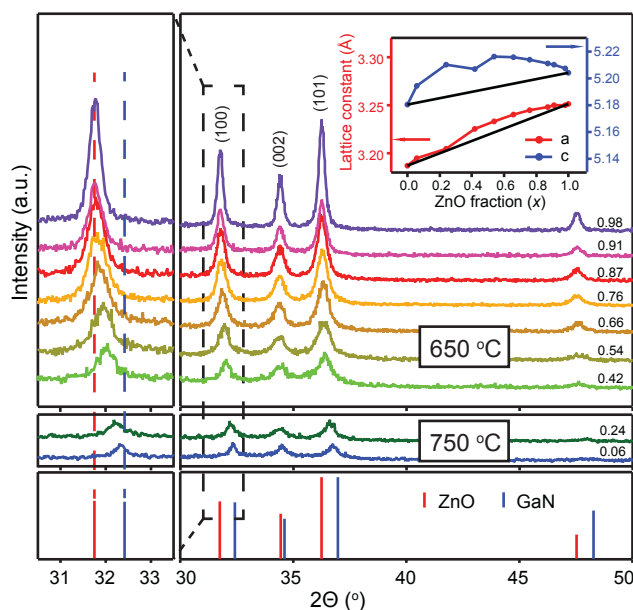

Figure 4. Powder XRD patterns of $(Ga_{1-x}Zn_x)(N_{1-x}O_x)$ with 0.06≤x≤0.98. The inset represents the variation of lattice parameters compared with the linear behavior expected from an ideal solid solution. The vertical lines represent the reference patterns for ZnO (red, JCPDS #05-0664), and GaN (blue, JCPDS # 2-1078).

2. $(Ga_{1-x}Zn_x)(N_{1-x}O_x)$ nanocrystals with a broad range of compositions

An improved understanding of the mechanism of formation of $(Ga_{1-x}Zn_x)(N_{1-x}O_x)$ nanocrystals allowed us to extend the range of x values from the previously reported 0.30 ≤x≤0.87 to each end of the range. Broadening the sample composition range then allowed us to examine how the visible absorption behaves as the composition approaches pure GaN or ZnO, both of which are UV absorbers. Figure 4 shows XRD patterns and lattice constants for the wurtzite $(Ga_{1-x}Zn_x)(N_{1-x}O_x)$ nanocrystal samples with x ranging from 0.06 to 0.98. For comparative purposes, this plot includes the XRD patterns of previously reported compositions (0.30≤x≤0.87).[32] The preparation of the samples at the two ends of the range is described below.

The composition of the starting material $ZnGa_2O_4$ suggests that if it converts to $(Ga_{1-x}Zn_x)(N_{1-x}O_x)$, the resulting x value would be ~0.3. This defines the lower limit on the x value without loss of Zn. As shown in Figure 1, significant increases in temperature are necessary to obtain good crystallinity from nitridation of $ZnGa_2O_4$ alone, at the cost of significant Zn evaporation. To aid material crystallinity, and remedy some of the loss of Zn so that there is continuous control of composition, we add extra ZnO and elevate the temperature to 750 ^{o}C for 10 hours to obtain $(Ga_{1-x}Zn_x)(N_{1-x}O_x)$ samples with low x values. The starting mixtures having Zn/(Zn+Ga) values of ~0.3 and 0.4 were nitrided at 750 ^{o}C for 10 hours, leading to the products with x values of 0.06 and 0.24, respectively. The XRD patterns of the products show a wurtzite phase, and the XRD peak positions approach the values of GaN with decreasing ZnO fraction (x), as shown in Figure 4. The TEM images of the low-x products show that the product consists of particles that are more agglomerated than those made at 650

ARTICLE

Journal Name

°C (Figure S4). It is possible that, with a low concentration of ZnO particles that aid in nucleation of $(Ga_{1-x}Zn_x)(N_{1-x}O_x)$, direct conversion of spinel $ZnGa_2O_4$ to wurtzite is prevalent.

At the other end of the composition range, it is straightforward to synthesize ZnO-rich $(Ga_{1-x}Zn_x)(N_{1-x}O_x)$ (*x*=0.91 and 0.98) by adding more ZnO into the starting mixture. The starting mixture was nitrided at 650 °C for 10 hours, as previously reported.[32] The XRD patterns of these samples indicate that the ZnO-rich products have wurtzite structure with XRD peak positions that approach those of ZnO with increasing *x* (Figure 4). The low-magnification TEM images show particles with average diameters of 20 nm for *x*=0.91 and 29 nm for *x*=0.98 (Figure S4), consistent with the narrowing of the XRD peaks for these high-*x* samples.

The lattice constants *c* and *a* calculated from the XRD patterns for the full range of compositions are shown in the inset of Figure 4. The presence of single peaks that range in position from those of GaN to those of ZnO are consistent with previous reports and are indicative of a solid solution rather than isolated domains of GaN and ZnO.[22, 25-27, 30, 36, 37] The linear behavior that would be expected for an ideal solid solution from Vegard's law is shown as the black line. Instead of the ideal behavior, we observe bowing that indicates that the $(Ga_{1-x}Zn_x)(N_{1-x}O_x)$ wurtzite lattice is slightly expanded. This behavior may be due to the non-isovalent nature of $(Ga_{1-x}Zn_x)(N_{1-x}O_x)$, and has been predicted and observed in bulk $(Ga_{1-x}Zn_x)(N_{1-x}O_x)$.[10, 26] The low-*x* samples prepared at 750 °C appear to have the lattice constant *a* close to the value for an ideal solid solution, but this is not the case for the lattice constant *c*. The small bowing of the lattice parameter *a* has also been observed in $(Ga_{1-x}Zn_x)(N_{1-x}O_x)$ hollow nanospheres.[36] The XPS data for several compositions (Figure S5) show a shift of lattice O and N with composition that is consistent with formation of Ga-O and Zn-N bonds in $(Ga_{1-x}Zn_x)(N_{1-x}O_x)$ nanocrystals, in agreement with XRD data in Figure 4.

In Figure 5, the diffuse reflectance spectra of the newly synthesized samples (*x*=0.06, 0.24, 0.92, and 0.98) are plotted together with the previously reported compositions (0.30≤*x*≤0.87).[32] For clarity, the spectra are separated according to composition with the range 0.06≤*x*≤0.66 shown in Figure 5a and 0.76≤*x*≤0.98 shown in Figure 5b. It is challenging to extract an accurate value for band gap energy (E_g) from the diffuse reflectance spectra of $(Ga_{1-x}Zn_x)(N_{1-x}O_x)$ because below-band gap absorption features (free carrier absorption and Urbach tail) are present in addition to the direct band gap transitions.[37] The contributions of these features to the diffuse reflectance spectra of nanocrystalline $(Ga_{1-x}Zn_x)(N_{1-x}O_x)$ are shown in Figure S6. The value of E_g determined from the Urbach tail and free carrier contributions is consistently lower, by 0.1–0.4 eV, than that determined from a Tauc plot for direct band gap absorption, as shown in Figure S6k. However, the E_g value from the absorption below the band gap is very sensitive to the fitting range and difficult to determine uniquely. Because of this uncertainty, we use the values of E_g determined from Tauc plots to examine how they vary with composition (Figure 5c). Based on the analysis in Figure S6, these values are upper limits on the true band gap. We note

that the composition-dependent behavior is independent of the band gap determination method (Figure S6k).
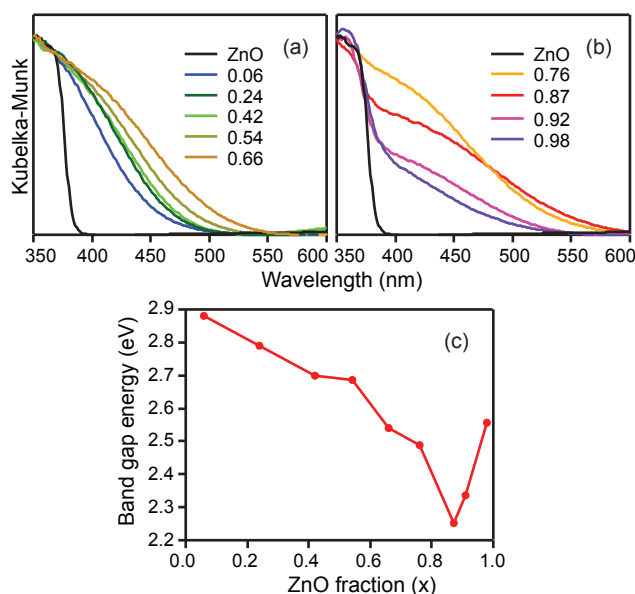

Figure 5. Diffuse reflectance spectra of $(Ga_{1-x}Zn_x)(N_{1-x}O_x)$ with varying composition with (a) *x*=0.06–0.66 and (b) *x*=0.76–0.98, along with that of ZnO. Spectra are normalized at 350 nm. (c) Band gap energies of the $(Ga_{1-x}Zn_x)(N_{1-x}O_x)$ products as a function of ZnO fraction (*x*).

As shown in Figure 5c, the value of E_g for $(Ga_{1-x}Zn_x)(N_{1-x}O_x)$ shifts to lower energy range with increasing *x* value from *x*=0.06 to *x*=0.87. Interestingly, the minimum E_g is found at *x*=0.87 (2.25 eV), and a blue shift is observed above *x*=0.87. An E_g value of 2.25 eV is of interest for solar fuel generation because a semiconductor with this band gap has a maximum achievable solar-to-H_2 conversion efficiency of 12%.[44] The products at each end (0.06 and 0.98) have E_g values of 2.9 and 2.6 eV, respectively. Considering the large band gap of GaN (3.4 eV) and ZnO (3.2 eV), very small compositional changes from the pure ZnO or GaN can cause a large band gap shift, as has been observed in $(Ga_{1-x}Zn_x)(N_{1-x}O_x)$ materials synthesized by other methods.[14, 25, 27, 30, 36, 37]

At the low-*x* end of the composition range, the diffuse reflectance spectra have similar shapes, with the effect of the composition being simply the red shifting of the spectrum (Figure 5a). At the high-*x* end of the range, however, both the band gap and the spectral shape change with composition (Figure 5b). The absorption at wavelengths below 390 nm characteristic of ZnO begins to emerge in the spectra of the ZnO-rich samples starting with *x*=0.76. This ZnO-like absorption becomes stronger compared to visible absorption with increasing *x*. The ZnO-like feature in the optical spectra of high-*x* $(Ga_{1-x}Zn_x)(N_{1-x}O_x)$ was also observed in $(Ga_{1-x}Zn_x)(N_{1-x}O_x)$ samples prepared from a combustion method.[25] Remarkably, the visible absorption is still relatively strong even when *x*=0.98, i.e., almost pure ZnO (Figure 5b). It is possible that at the very high *x* values, samples may contain some ZnO residue. However, we recently reported evidence that ZnO-like absorption can arise from $(Ga_{1-x}Zn_x)(N_{1-x}O_x)$ nanocrystals.[12] Transient absorption spectra of solubilized $(Ga_{1-x}Zn_x)(N_{1-x}O_x)$

nanocrystals with *x*=0.73 exhibit both visible and UV ZnO-like bleaches, and their decay traces overlap, indicating that they share electronic character.[12] These experimental observations are consistent with a model for the visible absorption that involves interband transitions between a higher lying valence band made by intermixing of ZnO and GaN orbitals and a conduction band that originates mostly from Zn and O orbitals.[5, 8, 12] The UV absorption would then originate from transitions from lower lying valence band levels to the same conduction band.[12] The spectra in Figure 5 are consistent with this picture, as a transition from a valence band that originates from compositional mixing to a conduction band that originates from ZnO would decrease in relative strength as the *x* value increases (i.e., GaN fraction decreases).
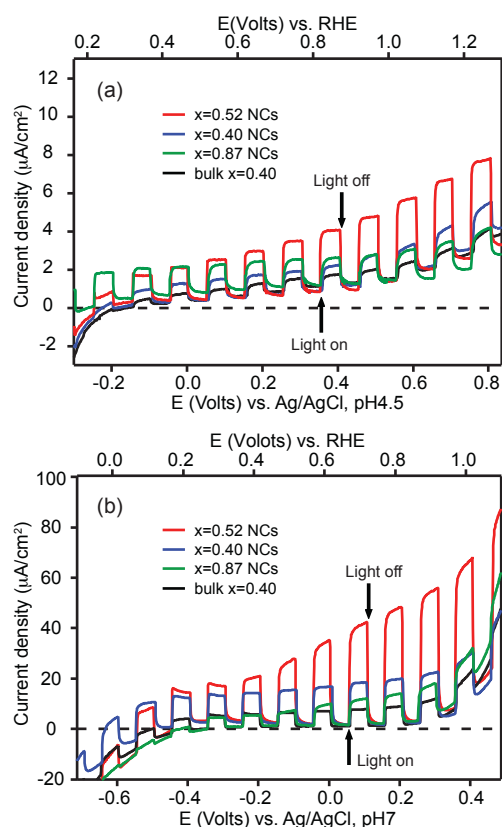

Figure 6. Current-voltage curves for films of bulk and nanoscale $(Ga_{1-x}Zn_x)(N_{1-x}O_x)$ (*x*=0.40 for bulk; *x*=0.40, 0.52, and 0.87 for nanocrystals) obtained from (a) Water oxidation in pH 4.5 0.5 M Na_2SO_4 aqueous solution and (b) Sulfite oxidation in pH 7 phosphate buffer solution with 0.5 M Na_2SO_3. Both were measured under illumination with λ>435 nm.

3. PEC activity of bulk and nanoscale $(Ga_{1-x}Zn_x)(N_{1-x}O_x)$

While visible absorption in $(Ga_{1-x}Zn_x)(N_{1-x}O_x)$ is encouraging for applications in solar fuel generation, it is important to examine the photoresponse of $(Ga_{1-x}Zn_x)(N_{1-x}O_x)$ nanocrystals. Bulk $(Ga_{1-x}Zn_x)(N_{1-x}O_x)$ has been shown to exhibit PEC activity under visible illumination. $(Ga_{1-x}Zn_x)(N_{1-x}O_x)$ thin films prepared by sputtering exhibit n-type behavior and show a reduced band gap with an improved photoresponse compared to ZnO and N-doped ZnO films.[45, 46] Stoichiometric H_2 and O_2 generation was achieved from PEC water splitting using bulk $(Ga_{1-x}Zn_x)(N_{1-x}O_x)$ on a FTO loaded with IrO_2 as a water

oxidation co-catalyst.[47] ZnO-rich $(Ga_{1-x}Zn_x)(N_{1-x}O_x)$ produced by solution combustion method generated visible driven photocurrent that was 30 times higher than for ZnO.[48] To assess the PEC behavior of our $(Ga_{1-x}Zn_x)(N_{1-x}O_x)$ nanocrystals, we compared them to bulk $(Ga_{1-x}Zn_x)(N_{1-x}O_x)$ prepared by the originally reported synthesis method.[14]

The current-voltage curves measured for films of bulk (*x*=0.40) and nanoscale (*x*=0.40, 0.52, and 0.87) $(Ga_{1-x}Zn_x)(N_{1-x}O_x)$ on FTO were measured in aqueous solution with 0.5 M Na_2SO_4 (Figure 6a). The experiments were carried out at pH 4.5 because the highest photocurrent for the bulk $(Ga_{1-x}Zn_x)(N_{1-x}O_x)$ in PEC oxidation was achieved at this pH.[47] The light source (300W Xe arc lamp) was passed through a 435 nm long pass filter to isolate the visible-light driven photo-response. Both the bulk and the nanocrystalline samples exhibit n-type behavior (Figure 6a). The bulk $(Ga_{1-x}Zn_x)(N_{1-x}O_x)$ (*x*=0.40) electrode produced photocurrents of 1–2 μA/cm^2 at 0.5 V, in agreement with previously reported results.[47, 49] Nanoscale $(Ga_{1-x}Zn_x)(N_{1-x}O_x)$ showed higher photocurrents by a factor of two and four for *x*=0.40 and *x*=0.52, respectively. Similar improvement in overall visible-driven water splitting when nanoscale $(Ga_{1-x}Zn_x)(N_{1-x}O_x)$ was used was reported in nanowires,[33] and, more recently, hollow nanospheres.[36]

The photocurrents observed in Figure 6a are quite low compared to the amount of light absorbed. The origin of the photocurrent may be water oxidation, or it may be due to other processes, such as semiconductor decomposition or sulfate oxidation. The samples are thick films (~50 μm in thickness), and carrier transport can limit the observed current.[57-59] More work is needed to understand the factors that determine the PEC behavior of films of $(Ga_{1-x}Zn_x)(N_{1-x}O_x)$ nanocrystals. Based on the strength of the visible absorption in solubilized $(Ga_{1-x}Zn_x)(N_{1-x}O_x)$ nanocrystals, we have recently shown that most of the incident visible light can be absorbed in a layer of $(Ga_{1-x}Zn_x)(N_{1-x}O_x)$ that is < 1μm thick.[12] Optimization of the device architecture may lead to higher photocurrent values.

Figure 6b shows that order of magnitude higher photocurrents can be detected for similar electrodes when they are immersed in pH 7 phosphate buffer solution with 0.5 M Na_2SO_3. This higher photocurrent can be attributed to sulfite oxidation, which is kinetically more favorable than water oxidation.[59, 60] The increase in photocurrent in the presence of sulfite suggests that the photocurrents in Figure 6a are at least partially limited by slow oxidation kinetics and that functionalization with oxidation catalysts could enhance PEC activity.[59] Similar observation was made in the case of bulk $(Ga_{1-x}Zn_x)(N_{1-x}O_x)$, where electrode functionalization with a water oxidation co-catalyst (IrO_2) led to an enhanced oxidation photocurrent and direct detection of water splitting products.[47]

Among the nanocrystalline $(Ga_{1-x}Zn_x)(N_{1-x}O_x)$ samples in Figure 6, observed photocurrents do not directly correlate with absorption of visible light (λ>435 nm). The *x*=0.52 sample absorbs 27% more of the visible photon flux than the *x*=0.40 sample, yet the observed photocurrents in Figure 6 are more than a factor of two higher. Similarly, the *x*=0.87 sample, which

exhibits the lowest band gap energy of all the samples, produces lower photocurrents than the x=0.52 sample, even though it absorbs 120% more of the λ>435 nm photons. The values of photocurrent depend on multiple factors, including charge transport efficiency, as well as the band edge potentials, which change with composition.[36, 50-56] IPCE spectra for sulfite oxidation provide some insight into the discrepancy between the ability to absorb visible light and the photocurrent produced (Figure S7). The x=0.52 sample shows highest IPCE values across the visible spectrum. Interestingly, the x=0.87 sample has an IPCE spectrum that resembles that of x=0.40 even though their band gaps differ by ~450 meV (Figure 5c). The lowest energy absorbed photons in the x=0.87 sample do not appear to contribute significantly to the photocurrent. Further work is necessary to understand the relationships between absorption and photocurrent spectra in $(Ga_{1-x}Zn_x)(N_{1-x}O_x)$ and to determine the composition that optimally balances absorption of sunlight with the other factors that govern photocurrent values.

Conclusions

We have characterized the properties of nanocrystalline $(Ga_{1-x}Zn_x)(N_{1-x}O_x)$ with a broad range of compositions, with emphasis on aspects relevant for solar water splitting applications. Examination of the synthetic procedure for $(Ga_{1-x}Zn_x)(N_{1-x}O_x)$ nanocrystals suggests that $(Ga_{1-x}Zn_x)(N_{1-x}O_x)$ nucleates topotactically at the interface of ZnO and $ZnGa_2O_4$ nanocrystals. Manipulating the synthetic parameters allows us to obtain a very broad range of sample compositions, $0.06 \leq x \leq 0.98$, and to examine how the optical spectra vary with composition. While visible absorption is achieved even in samples close to x=0 (GaN) and x=1 (ZnO), the minimum band gap of 2.25 eV occurs at x=0.87. Finally, we find that films of $(Ga_{1-x}Zn_x)(N_{1-x}O_x)$ nanocrystals are photoactive for PEC oxidation, although with low photocurrents. The availability and optical characterization of $(Ga_{1-x}Zn_x)(N_{1-x}O_x)$ nanocrystals with a broad composition range sets the stage for the investigation of these materials for visible-light driven water oxidation.

Acknowledgements

Notes and references

1. K. Maeda, T. Takata, M. Hara, N. Saito, Y. Inoue, H. Kobayashi and K. Domen, *J. Am. Chem. Soc.*, 2005, **127**, 8286-8287.
2. T. Hirai, K. Maeda, M. Yoshida, J. Kubota, S. Ikeda, M. Matsumura and K. Domen, *J. Phys. Chem. C*, 2007, **111**, 18853-18855.
3. L. L. Jensen, J. T. Muckerman and M. D. Newton, *J. Phys. Chem. C*, 2008, **112**, 3439-3446.
4. W. Wei, Y. Dai, K. Yang, M. Guo and B. Huang, *J. Phys. Chem. C*, 2008, **112**, 15915-15919.
5. M. N. Huda, Y. Yan, S.-H. Wei and M. M. Al-Jassim, *Phys. Rev. B*, 2008, **78**, 195204.
6. S. Wang and L.-W. Wang, *Phys. Rev. Lett.*, 2010, **104**, 065501.
7. M. Yashima, H. Yamada, K. Maeda and K. Domen, *Chem. Commun.*, 2010, **46**, 2379-2381.
8. C. Di Valentin, *J. Phys. Chem. C*, 2010, **114**, 7054-7062.
9. M. Yoshida, T. Hirai, K. Maeda, N. Saito, J. Kubota, H. Kobayashi, Y. Inoue and K. Domen, *J. Phys. Chem. C*, 2010, **114**, 15510-15515.
10. L. Li, J. T. Muckerman, M. S. Hybertsen and P. B. Allen, *Phys. Rev. B*, 2011, **83**, 134202.
11. E. J. McDermott, E. Z. Kurmaev, T. D. Boyko, L. D. Finkelstein, R. J. Green, K. Maeda, K. Domen and A. Moewes, *J. Phys. Chem. C*, 2012, **116**, 7694-7700.
12. C.-H. Chuang, Y.-G. Lu, K. Lee, J. Ciston and G. Dukovic, *J. Am. Chem. Soc.*, 2015, **137**, 6452-6455.
13. K. Maeda, K. Teramura, T. Takata, M. Hara, N. Saito, K. Toda, Y. Inoue, H. Kobayashi and K. Domen, *J. Phys. Chem. B*, 2005, **109**, 20504-20510.
14. K. Maeda, K. Teramura, D. Lu, T. Takata, N. Saito, Y. Inoue and K. Domen, *Nature*, 2006, **440**, 295-295.
15. K. Maeda, K. Teramura, D. Lu, T. Takata, N. Saito, Y. Inoue and K. Domen, *J. Phys. Chem. B*, 2006, **110**, 13753-13758.
16. K. Maeda, K. Teramura, H. Masuda, T. Takata, N. Saito, Y. Inoue and K. Domen, *J. Phys. Chem. B*, 2006, **110**, 13107-13112.
17. K. Maeda and K. Domen, *J. Phys. Chem. C*, 2007, **111**, 7851-7861.
18. K. Maeda, H. Hashiguchi, H. Masuda, R. Abe and K. Domen, *J. Phys. Chem. C*, 2008, **112**, 3447-3452.
19. K. Maeda, K. Teramura and K. Domen, *J. Catal.*, 2008, **254**, 198-204.
20. T. Hisatomi, K. Maeda, D. Lu and K. Domen, *ChemSusChem*, 2009, **2**, 336-343.
21. T. Hisatomi, K. Maeda, K. Takanabe, J. Kubota and K. Domen, *J. Phys. Chem. C*, 2009, **113**, 21458-21466.
22. K. Maeda and K. Domen, *Chem. Mater.*, 2010, **22**, 612-623.
23. T. Ohno, L. Bai, T. Hisatomi, K. Maeda and K. Domen, *J. Am. Chem. Soc.*, 2012, **134**, 8254-8259.
24. H. Chen, W. Wen, Q. Wang, J. C. Hanson, J. T. Muckerman, E. Fujita, A. I. Frenkel and J. A. Rodriguez, *J. Phys. Chem. C*, 2009, **113**, 3650-3659.
25. M. Mapa, K. S. Thushara, B. Saha, P. Chakraborty, C. M. Janet, R. P. Viswanath, C. Madhavan Nair, K. V. G. K. Murty and C. S. Gopinath, *Chem. Mater.*, 2009, **21**, 2973-2979.
26. H. Chen, L. Wang, J. Bai, J. C. Hanson, J. B. Warren, J. T. Muckerman, E. Fujita and J. A. Rodriguez, *J. Phys. Chem. C*, 2010, **114**, 1809-1814.
27. J. Wang, B. Huang, Z. Wang, P. Wang, H. Cheng, Z. Zheng, X. Qin, X. Zhang, Y. Dai and M.-H. Whangbo, *J. Mater. Chem.*, 2011, **21**, 4562-4567.
28. A. Kay, I. Cesar and M. Grätzel, *J. Am. Chem. Soc.*, 2006, **128**, 15714-15721.

29. E. M. Sabio, R. L. Chamousis, N. D. Browning and F. E. Osterloh, *J. Phys. Chem. C*, 2012, **116**, 3161-3170.

30. W.-Q. Han, Z. Liu and H.-G. Yu, *Appl. Phys. Lett.*, 2010, **96**, 183112.

31. W.-Q. Han, Y. Zhang, C.-Y. Nam, C. T. Black and E. E. Mendez, *Appl. Phys. Lett.*, 2010, **97**, 083108.

32. K. Lee, B. M. Tienes, M. B. Wilker, K. J. Schnitzenbaumer and G. Dukovic, *Nano Lett.*, 2012, **12**, 3268-3272.

33. C. Hahn, M. A. Fardy, C. Nguyen, M. Natera-Comte, S. C. Andrews and P. Yang, *Isr. J. Chem.*, 2012, **52**, 1111-1117.

34. B. Liu, Y. Bando, L. Liu, J. Zhao, M. Masanori, X. Jiang and D. Golberg, *Nano Lett.*, 2013, **13**, 85-90.

35. M. Zhong, Y. Ma, P. Oleynikov, K. Domen and J.-J. Delaunay, *Energy Environ. Sci.*, 2014, **7**, 1693-1699.

36. Y. Li, L. Zhu, Y. Yang, H. Song, Z. Lou, Y. Guo and Z. Ye, *Small*, 2015, **11**, 871-876.

37. A. A. Reinert, C. Payne, L. Wang, J. Ciston, Y. Zhu and P. G. Khalifah, *Inorg. Chem.*, 2013, **52**, 8389-8398.

38. V. B. Ram Boppana, D. J. Doren and R. F. Lobo, *J. Mater. Chem.*, 2010, **20**, 9787-9797.

39. V. B. Ram Boppana, H. Schmidt, F. Jiao, D. J. Doren and R. F. Lobo, *Chem. Eur. J.*, 2011, **17**, 12417-12428.

40. X. Sun, K. Maeda, M. Le Faucheur, K. Teramura and K. Domen, *Appl. Catal.,*, 2007, **327**, 114-121.

41. A. R. West, *Basic Solid State Chemistry*, John Wiley & Sons, Ltd, New York, 2nd edn., 1999.

42. N. Kumagai, L. Ni and H. Irie, *Chem. Commun.*, 2011, **47**, 1884-1886.

43. V. Srikant and D. R. Clarke, *J. Appl. Phys.*, 1998, **83**, 5447-5451.

44. Z. Chen, T. F. Jaramillo, T. G. Deutsch, A. Kleiman-Shwarscstein, A. J. Forman, N. Gaillard, R. Garland, K. Takanabe, C. Heske, M. Sunkara, E. W. McFarland, K. Domen, E. L. Miller, J. A. Turner and H. N. Dinh, *J. Mater. Res.*, 2010, **25**, 3-16.

45. S. Shet, Y. Yan, J. Turner and M. Al-Jassim, *J. Power Sources*, 2013, **232**, 74-78.

46. K.-S. Ahn, Y. Yan, S. Shet, T. Deutsch, J. Turner and M. Al-Jassim, *Appl. Phys. Lett.*, 2007, **91**, 231909.

47. H. Hashiguchi, K. Maeda, R. Abe, A. Ishikawa, J. Kubota and K. Domen, *Bull. Chem. Soc. Jpn.*, 2009, **82**, 401-407.

48. S. RajaAmbal, A. K. Yadav, S. N. Jha, D. Bhattacharyya and C. S. Gopinath, *Phys. Chem. Chem. Phys.*, 2014, **16**, 23654-23662.

49. K. Maeda, A. Xiong, T. Yoshinaga, T. Ikeda, N. Sakamoto, T. Hisatomi, M. Takashima, D. Lu, M. Kanehara, T. Setoyama, T. Teranishi and K. Domen, *Angew. Chem., Int. Ed.*, 2010, **49**, 4096-4099.

50. M. Zhou, J. Bao, Y. Xu, J. Zhang, J. Xie, M. Guan, C. Wang, L. Wen, Y. Lei and Y. Xie, *ACS Nano*, 2014, **8**, 7088-7098.

51. K. Sivula, R. Zboril, F. Le Formal, R. Robert, A. Weidenkaff, J. Tucek, J. Frydrych and M. Grätzel, *J. Am. Chem. Soc.*, 2010, **132**, 7436-7444.

52. Y. J. Hwang, C. H. Wu, C. Hahn, H. E. Jeong and P. Yang, *Nano Lett.*, 2012, **12**, 1678-1682.

53. Y. Li, T. Takata, D. Cha, K. Takanabe, T. Minegishi, J. Kubota and K. Domen, *Adv. Mater.*, 2013, **25**, 125-131.

54. S. Sunkara, V. K. Vendra, J. B. Jasinski, T. Deutsch, A. N. Andriotis, K. Rajan, M. Menon and M. Sunkara, *Adv. Mater.*, 2014, **26**, 2878-2882.

55. N. Chouhan, R.-S. Liu and S.-F. Hu, *J. Mater. Chem. A*, 2013, **1**, 7422-7432.

56. G. Zhang, D. Monllor-Satoca and W. Choi, *Catal. Sci. Technol.*, 2013, **3**, 1790-1797.

57. W. H. Leng, P. R. F. Barnes, M. Juozapavicius, B. C. O'Regan and J. R. Durrant, *J. Phys. Chem. Lett.*, 2010, **1**, 967-972.

58. Y. Qiu, S.-F. Leung, Q. Zhang, B. Hua, Q. Lin, Z. Wei, K.-H. Tsui, Y. Zhang, S. Yang and Z. Fan, *Nano Lett.*, 2014, **14**, 2123-2129.

59. J. A. Seabold, K. Zhu and N. R. Neale, *Phys. Chem. Chem. Phys.*, 2014, **16**, 1121-1131.

60. W. Liu, H. Ye and A. J. Bard, *J. Phys. Chem. C*, 2010, **114**, 1201-1207.